Chinese Chemical Letters 37 (2026) 112540

Contents lists available at ScienceDirect

Chinese Chemical Letters

journal homepage: www.elsevier.com/locate/cclet

Constructing H_2O-locking structure of the double hydrogen bond network for reversible zinc metal anode

Yang Yu[a,b,1], Yi-Yang Bi[a,1], Yu-Hang Liu[a], Bin Yue[b], Ming-Xuan Duan[a], Yu-Chun Wan[a,*], Wan-Qiang Liu[a,*], Gang Huang[c,*]

[a] School of Materials Science and Engineering, Changchun University of Science and Technology, Changchun 130000, China
[b] School of Chemistry, Tonghua Normal University, Tonghua 134000, China
[c] State Key Laboratory of Rare Earth Resource Utilization, Changchun Institute of Applied Chemistry, Chinese Academy of Sciences, Changchun 130022, China

ARTICLE INFO

Article history:
Received 19 January 2026
Revised 26 January 2026
Accepted 23 February 2026
Available online 23 February 2026

Keywords:
Zinc metal anode
Aqueous zinc-ion batteries
Dendrite suppression
Double H-bond H_2O-locking structure
Uniform deposition

ABSTRACT

Zinc anode as one of the most promising energy storage materials for aqueous zinc-ion batteries (AZIBs), suffer from significant degradation in cycle life and Coulombic efficiency (CE) due to uncontrolled dendrite growth and H_2O-induced side reactions. In this work, we propose a nonionic dual-additive (gelatin, urea, abbreviated as GU) strategy that utilizes the dual hydrogen bond (H-bond) network H_2O-locking structure. Due to the H-bond reinforcement effect introduced by the GU additive, the energy barrier for H-bond breaking and reconfiguration is elevated, effectively impeding the rapid proton shuttling between H_2O molecules. It can induce the preferred growth of the (002) crystal plane by adsorbing onto other crystal planes, thereby achieving a dendrite-free zinc anode. Thus, the stability and reversibility of the zinc anode have improved significantly. The symmetrical cells stably cycled for more than 2100 h at 2.0 mA/cm^2@1.0 mA/cm^2, and the Zn||Cu asymmetric cells cycled for 1600 times at 5 mA/cm^2@1 mAh/cm^2 with an average CE of 99.4 %. The full cells matched with the PANI cathode cycled more than 3500 times at 1 A/g. The work provides a new strategy for regulating the interfacial chemistry of zinc anodes to achieve highly stable high-performance zinc batteries.

© 2026 Published by Elsevier B.V. on behalf of Chinese Chemical Society and Institute of Materia Medica, Chinese Academy of Medical Sciences.

Aqueous zinc-ion batteries (AZIBs) have attracted attention due to their high safety, low cost, non-toxicity and high theoretical zinc capacity (820 mAh/g or 5855 mAh/cm^3) [1–4]. However, the zinc anode is unstable and has low reversibility during deposition/stripping due to the issues such as dendrite growth, hydrogen evolution reaction (HER), and corrosion, which hinders its commercialization [5,6]. The intrinsic surface defects of the zinc anode lead to an uneven electric field and Zn^{2+} flux, promoting dendrite growth at tips and internal short circuits. Concurrently, Zn^{2+} solvation with water triggers local pH increase and the generation of by-products [7–9]. These by-products exacerbate the uneven deposition of Zn^{2+}, resulting in "dead zinc". More imminently, the unfavorable dendritic growth and insufficient interfacial protection, which are mostly brought on by the uneven surface morphology of zinc deposition, easily pass through the separator during repeated electrochemical tests and eventually result in irreversible device failure [10–13]. Severe water-induced corrosion and HER that curtail cycle life and rate performance [14–16].

Traditional mitigation strategies, such as high-concentration electrolytes and interface modification strategies, to some extent compromise cost, kinetic performance, and safety [17,18]. Consequently, various strategies have been proposed to resolve or alleviate these challenges, including an effective strategy to stabilize zinc anode electrode is to inhibit H_2O activity in aqueous electrolyte. The risk of H_2O decomposition stems from its triggering of a HER within the electric double layer (EDL), resulting in local disturbances during zinc deposition. Specifically, hydrated zinc ions desolvate at the outer Helmholtz plane (OHP) and promote charge transfer at the inner Helmholtz plane (IHP), resulting in zinc deposition [19]. According to the principle of minimum energy consumption, zinc tends to form an aggregate state during diffusion and deposition, resulting in dendrite formation. At the same time, H_2O molecules continue to migrate from OHP to IHP, exacerbating HER process through H_2O decomposition on the zinc negative surface. In addition to inhibiting HER, the construction of stable and high-quality artificial SEI layers has also been extensively studied because its structure and composition significantly affect the deposition behavior of zinc metals [20,21].

* Corresponding authors.
E-mail addresses: wanyuchun@126.com (Y.-C. Wan), wqliu1979@126.com (W.-Q. Liu), ghuang@ciac.ac.cn (G. Huang).
[1] These authors contributed equally to this work.

https://doi.org/10.1016/j.cclet.2026.112540
1001-8417/© 2026 Published by Elsevier B.V. on behalf of Chinese Chemical Society and Institute of Materia Medica, Chinese Academy of Medical Sciences.

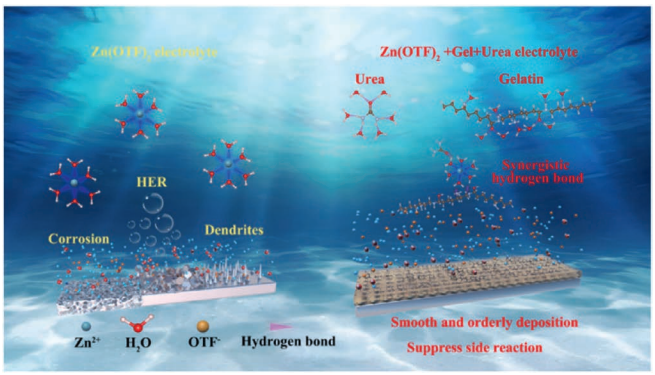


Fig. 1. Schematic representation of the deposition mechanism of Zn in different electrolytes. Schematic diagram showing the Zn anode status in a $Zn(OTf)_2$ and $Zn(OTf)_2$+Gel+Urea ($Zn(OTf)_2$/GU). (Left) Dendritic formation and hydrogen evolution occurred upon cycling. (Right) Smooth deposition was achieved with the aid of gel and urea dual-additives.

Typical electrolyte additives for AZIBs include organic molecules and inorganic/organic salts (*e.g.*, ionic liquids) with associated hydrophilic functional groups [22]. Unlike organic small molecules, organic macromolecules not only inhibit dendrite growth by modulating the Zn^{2+} cluster structure in the conventional electrolyte $ZnSO_4$. Their flexible long-chain/host-guest structure helps to modulate the zinc anode surface, except in the presence of strong organic acids/amines, whose functional groups typically dissociate at low pH [23]. Inorganic/organic salt additives in $ZnSO_4$ are highly dissociated into polar anions (*e.g.*, inhibiting zinc dendrite growth by shielding the zinc surface tip or compensating for electrons in the electrolyte carrier). These ions are highly polar and interact strongly with the charged Zn^{2+} ions. Effective zinc anodic deposition/etching in $ZnSO_4$ requires proper Zn^{2+} desolvation and solvation energies [24,25]. Therefore, H-bond acceptors in the electrolyte additives that are coordinated to Zn^{2+} or Zn are essential for a reversible deposition/stripping process. Ideal additives should be able to inhibit the electrochemical activity of Zn dendrites and H_2O in the IHP while maintaining the fast reaction kinetics of the zinc anode to ensure long cycle life at high currents [26].

Consequently, designing an effective approach to achieving notable advances in the regulation of electrolyte with high structural toughness and conductivity is essential for the long-term performance of AZIBs technology [27–29]. In this study, we report a highly efficient additive of N, O receptors with a double H-bond network structure and non-ionizing properties, which are used as electrolytes in AZIBs [30]. It is different from other organic molecular additives or salt additives [31]. The coordination ability of N in the modified H-bond network, where the O acceptor with a donor (such as Zn^{2+}/H_2O) is theoretically located between the organic molecule and the ionic acceptor, allows Zn^{2+} to achieve an appropriate desolvation/solvation energy to uniformly stripping/plating the Zn anode while inhibiting IHP. The results of H_2O activity in it indicate that the Zn||Zn symmetrical battery using the optimized $Zn(OTf)_2$ electrolyte exhibits excellent cycling stability (up to 2160 h at a current density of 2 mA/cm^2 and a capacity of 1 mAh/cm^2). In AZIBs, gelatin and urea (GU), as composite additives, which can effectively inhibit the activity of free H_2O in the electrolyte by synergistic construction of a dynamic H-bond network H_2O-locking structure, thereby reducing side reactions (such as HER and zinc corrosion). The mechanism of action as shown in Fig. 1. The -NH_2 (donor) and C=O (acceptor) in the urea molecule can respectively form multiple H-bond with H_2O molecules (each urea molecule can combine with a maximum of 4 H_2O molecules), forming a stable hydrated shell layer. By binding H_2O molecules through competitive H-bond, the direct contact between free H_2O and the Zn surface is reduced, and the hydrolysis side reactions are inhibited. The amino acid chains of gelatin (containing -OH, -COOH, -NH_2) are cross-linked with the urea-H_2O complex through H-bond to form a dynamic gelatin (gel)-like structure. The hydrophobic micro-regions of gel (such as proline residues) can repel free water and further isolate active H_2O molecules. The long chains of the gel network physically prevent dendrite growth, while the H-bond network regulates the Zn solvation structure, promotes uniform deposition, and inhibits side reactions.

To analyze the influence of the electrolyte on the zinc anode, the contact angle test of the electrolyte on the Zn anode is shown in Fig. S1 (Supporting information). The value in pure $Zn(OTf)_2$ electrolyte is 73.5°, while in $Zn(OTf)_2$/GU electrolyte the contact angle value is 62.3°. These experimental results indicate that, when GU are added to the electrolyte, the affinity between the electrolyte and the Zn anode increases, which is conducive to reversible galvanizing/stripping at the anode-electrolyte interface. The values of the contact angle bar graphs of different electrolytes are presented in Fig. S2 (Supporting information). Fig. 2a shows the results of local environment of the electrolyte using nuclear magnetic resonance (NMR) technology. After adding GU to the $Zn(OTf)_2$ electrolyte, the ^{1}H peak shifted from 4.83 ppm to 4.9 ppm. This is attributed to the formation of $Zn(H_2O)_6$ and the reduction in the electron density around the protons in the H_2O molecule [32,33]. The introduction of GU causes the ^{1}H peak to shift towards higher magnetic fields, indicating the formation of a new H-bond network between GU and H_2O molecules. This change results from cosolvents and H_2O forming more intermolecular H-bond, which breaks the network of H-bond connections that already existed between H_2O molecules. By preventing adverse interactions at the electrolyte/electrode contact, this variation is advantageous. The FT-IR spectrum shows characteristic peaks at 1632 cm^{-1} (assignable to C=O stretching), 1220 cm^{-1} (-CONH bending), and 1030 cm^{-1} (C-C stretching). These vibration modes indicate strong chemical coordination within the gel. The significant change in the O-H stretching vibration band (3000-3500 cm^{-1}) shown in Fig. 2b, serves as evidence for the reconstruction of the original hydrogen-bond network. Raman spectroscopy was used to investigate in order to have a better understanding of the electrolyte's condition in Fig. 2c. Raman spectral shifts, the red shift and changes in full width at half maximum (FWHM) of the O-H stretching vibration peak (~3400 cm^{-1}) of H_2O molecules surrounding Zn^{2+} serve as direct evidence for the perturbation and weakening of the hydrogen-bond network within the solvation sheath. This observation aligns with the mechanism of competitive hydrogen bonding between GU molecules, $Zn^{2+}$and H_2O. Considering both FT-IR and Raman spectra analysis, the oscillation spectra between 3000 cm^{-1} and 3500 cm^{-1} significantly display weak and narrow peak bands, indicating maximum utilization of the hydrophilic functional groups within the region and adequate chemical co-ordination networks during polymer building matrix. As depicted in Fig. 2d, the energy levels of the highest occupied molecular orbital (HOMO) and the lowest unoccupied molecular orbital (LUMO) of Gel molecules and H_2O molecules were carried out. The results show that the HOMO energy level of the Gel molecules (-6.35 eV) exceeds the highest occupied molecular orbital of H_2O (-8.61 eV). This indicates that electrons are more likely to transfer from Gel to the surface of the Zn anode after adsorption [34]. The adsorption energy of Gel molecules on different Zn crystal planes is determined through density functional theory (DFT) calculations (Fig. 2e). The structural model shown in Figs. S3-S5 (Supporting information) indicates that the adsorption energy of Gel molecules on the Zn (002) crystal plane reaches -3.28365 eV, which is significantly higher than that on the Zn (100) (-2.64099 eV) and Zn (101) crystal planes (-2.88271 eV). This result confirmed that Gel molecules have a stronger adsorption capacity on the Zn (002)

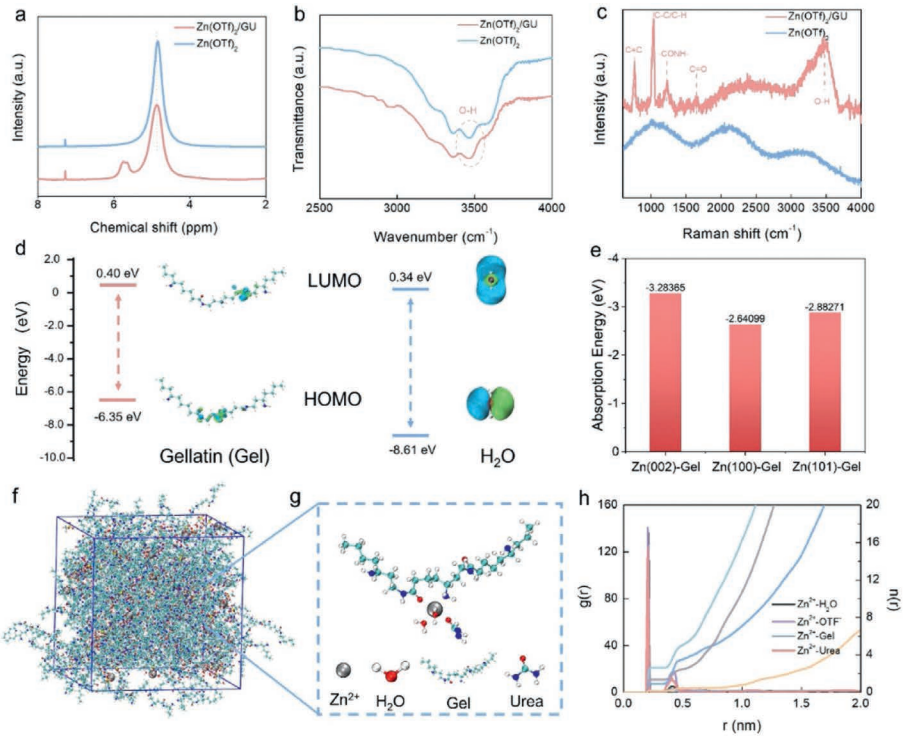


Fig. 2. (a) ^{1}H NMR spectra of the $Zn(OTf)_2$ and $Zn(OTf)_2$/GU electrolytes. (b) FT-IR spectra of the $Zn(OTf)_2$ and $Zn(OTf)_2$/GU electrolytes. (c) Raman spectra of the $Zn(OTf)_2$ and $Zn(OTf)_2$/GU electrolytes. (d) LUMO, HOMO isosurfaces of Gel and H_2O. (e) Comparison of the absorption energy of Gel on different Zn crystalline planes. (f, g) 3D snapshots of the electrolytes and typical solvation structures in $Zn(OTf)_2$/GU electrolytes obtained by MD simulations. (h) The RDFs and CN of Zn^{2+}-H_2O, Zn^{2+}-OTF^-, Zn^{2+}-Gel and Zn^{2+}-Urea collected from MD simulations in $Zn(OTf)_2$/GU electrolytes.

crystal plane. This excellent adsorption property is conducive to achieving more uniform and dense Zn deposition during the plating/stripping process. In order to further study the structural evolution of the solvated sheath layer at the molecular level, molecular dynamics (MD) simulations were first conducted to compare the solvated structure of hydrated Zn^{2+} in the Gel mixed electrolyte system [35]. Gel molecules and urea molecules additives enter the primary solvation structure of hydrated Zn^{2+}. Due to their superior zinc affinity, they may replace some H_2O molecules from the primary solvation sheath (Figs. 2f and g). Importantly, the results show that Gel molecules and urea molecules additives can change the solvation sheath layer of hydrated Zn^{2+} ions by partially replacing the coordinating H_2O molecules. Gel and urea molecules can participate in the first solvation structure of Zn^{2+} ions and reduce the number of ligand H_2O molecules. The Radial distribution function (RDF) in Fig. 2h indicates that the first solvation peak of Zn^{2+} is at 0.208 nm and the first solvation peaks of Zn^{2+}-OTf^-, Zn^{2+}-Gel, Zn^{2+}-urea are all 0.204, and the coordination number (ACN) of Zn^{2+}-H_2O is 2.633, Zn^{2+}-OTf^- is 0.9, Zn^{2+}-Gel is 1.367, Zn^{2+}-urea is 0.133. It indicates that enter the first solvation structure of Zn^{2+} ions to participate in coordination further demonstrating the existence of the coordination mechanism [36]. Meanwhile, the differential charge density indicates in Figs. S6-S8 (Supporting information) that there is a strong interaction between Gel molecules and the Zn surface, and Gel molecules have more charge transfer sites on the (002) crystal plane of Zn. This theoretical calculation result shows that there are more charge transfer sites between the (002) crystal plane of Zn and Gel, thus the combination is tighter [37].

Further, we assembled Zn||Cu and Zn||Zn cells to investigate the plating/stripping behaviors of Zn anodes in $Zn(OTf)_2$ and $Zn(OTf)_2$/GU electrolytes, respectively. The impact of GU additive on the Zn deposition kinetics was investigated *via* CV measurements (Fig. 3a). After the introduction of GU, compared with the pure $Zn(OTf)_2$ electrolyte, the nucleation overpotential increased by 34 mV. At higher nucleation overpotential, the nucleation radius of the grains was smaller, and the nucleation formation probability was higher. Therefore, during the subsequent Zn^{2+} deposition process, more and smaller nuclei could be formed, which is conducive to the uniform deposition of zinc ions on the zinc foil surface. This indicates that the introduction of GU has optimized the deposition process of zinc ions on the zinc foil surface and more homogeneous and finer zinc particles are formed [38,39]. In addition, the reversibility of the Zn plating/stripping process was evaluated by means of an asymmetric Zn||Cu cell. In $Zn(OTf)_2$/GU electrolyte the Zn||Cu half-cell exhibited an average Coulombic efficiency (CE) of 99.71 % nearly 1600 cycles, at 5 mA/cm^2, 1 mAh/cm^2 (Fig. 3b). A high CE indicates a stable electrode-electrolyte interface, significant suppression of byproducts, and highly reversible zinc anode deposition/dissolution behavior. In contrast, the Zn||Cu half-cell could not operate effectively after 70 cycles due to the fluctuation of the CE, at 1 mA/cm^2, 1 mAh/cm^2 (Fig. S9 in Supporting information) 880 cycles, which is attributed to the continuous growth of Zn dendrites and unwanted side reactions [40]. EIS measurements (Fig. 3c) of pure $Zn(OTf)_2$ and $Zn(OTf)_2$/GU electrolytes show that the charge transfer resistance of the Zn||Zn symmetric cell in $Zn(OTf)_2$/GU electrolytes is significantly smaller, confirming the fast electron transfer capability, which is conducive to the reduction of concentration polarisation and the achievement of a homogeneous distribution of Zn^{2+} during the Zn stripping/plating process. The voltage-capacity curves of Zn deposited in pure $Zn(OTf)_2$ and $Zn(OTf)_2$/GU electrolytes (Figs. S10 and S11 in Supporting information). Furthermore, the reversibility of Zn plating/stripping is evaluated using asymmetric Zn||Cu cells. The low polarization of the Zn||Cu half-cell at 1 mA/cm^2 and 1 mAh/cm^2 during 880 cycles was 111.9 mV.

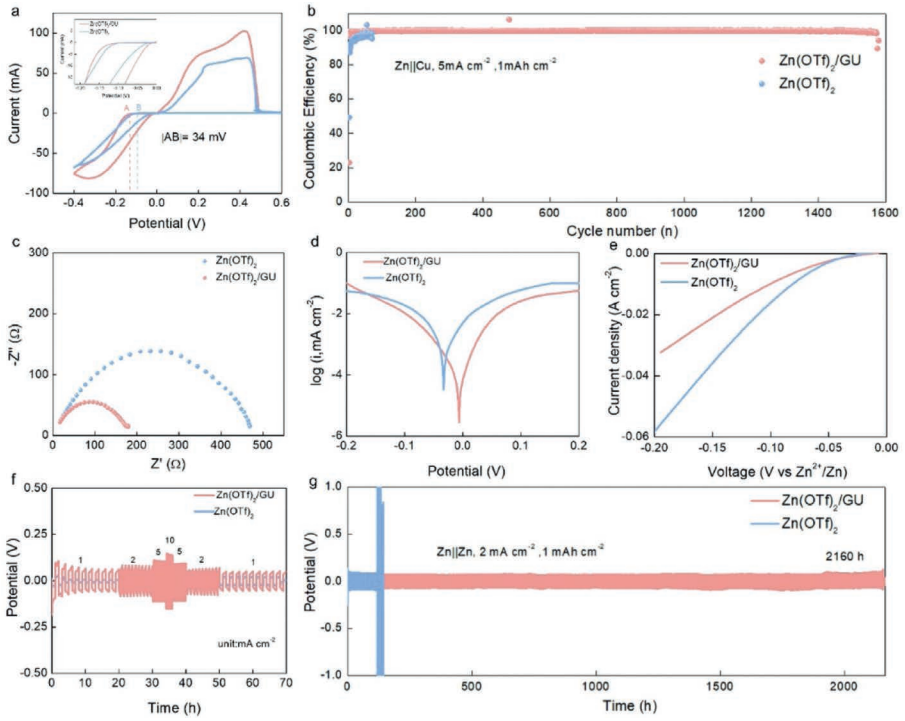


Fig. 3. (a) Cyclic voltammetry (CV) curves of Zn-Cu asymmetrical cells in $Zn(OTf)_2$ and $Zn(OTf)_2$/GU electrolytes. (b) CE of Zn-Cu asymmetrical cells operated at 5 mA/cm^2, 1mAh/cm^2. (c) EIS plots, (d) Tafel plots, (e) LSV plots of the $Zn(OTf)_2$ and $Zn(OTf)_2$/GU Zn||Zn symmetric cells. (f) Rate performance of Zn||Zn symmetric cells with $Zn(OTf)_2$ and $Zn(OTf)_2$/GU electrolytes. (g) Galvanostatic cycling of the Zn||Zn cells with the $Zn(OTf)_2$ and $Zn(OTf)_2$/GU electrolytes at a current density of 2 mA/cm^2 and a capacity of 1 mAh/cm^2.

In contrast, the Zn||Cu half-cell failed to function effectively after 108 cycles due to CE fluctuations, with a charge and discharge voltage gap of 67.6 mV. This was caused by the continuous growth of zinc dendrites and adverse side reactions. The impact of GU on corrosion inhibition was investigated using Tafel plots (Fig. 3d). When GU was added, the electrode's corrosion potential (Ecorr) decreased in comparison to the pure $Zn(OTf)_2$ electrolyte, suggesting that the electrode's corrosion was prevented and its rate of self-corrosion decreased. Additionally, the inhibitory action of HER decreased electrode surface corrosion. This demonstrates that GU has a beneficial effect in preventing corrosion-related side reactions. The liner scan voltammetry (LSV) is performed, as displayed in Fig. 3e, the GU containing electrolyte exhibits more negative overpotential than the pure $Zn(OTf)_2$ electrolyte, further validate this improvement, showing significantly HER activity in the GU-modified electrolytes. The current density evolution of the Zn||Zn symmetrical cell employing $Zn(OTf)_2$ electrolyte (Fig. S12 in Supporting information), the current density exhibits a continuous increase over 800 s, suggesting a progressive expansion of the effective surface area of the Zn anode. This behavior can be attributed to the predominance of an uncontrolled 2D diffusion process at the electrode/electrolyte interface. In such a regime, Zn^{2+} ions preferentially adsorb and migrate along the surface, leading to random nucleation and uneven nucleation site distribution. The sustained 2D diffusion promotes preferential Zn accumulation at existing protrusions, which gradually develops into dendritic structures. In contrast, the cell employing the $Zn(OTf)_2$/GU electrolyte shows clearly different behavior. After an initial 2D-dominated period (~55 s), the current density stabilizes, indicating a transition to a steady-state deposition process governed by 3D diffusion from the bulk electrolyte. This 3D diffusion controlled mode favors more uniform nucleation across the electrode surface and helps maintain a planar growth front. Consequently, this mechanism facilitates the formation of a homogeneous, compact, and smooth Zn deposition, effectively suppressing dendritic growth. Owing to the dual hydrogen-bonding capability of the GU additive, which effectively confines H_2O molecules within the electrolyte, the interfacial stability of the Zn anode is significantly enhanced. This improvement suppresses parasitic side reactions and promotes highly reversible Zn plating/stripping behavior during long-term cycling. The rate capability and cycling stability of Zn||Zn symmetric cells were systematically evaluated. Rate capability tests were systematically performed across current densities ranging from 1 mA/cm^2 to 10 mA/cm^2 and with an area capacity of 1 mAh/cm^2 to further conducted to evaluate the zinc plating/stripping efficiency (Fig. 3f). Obviously, the Zn||Zn symmetrical cells tested in pure $Zn(OTf)_2$ electrolyte failed rapidly a short circuit occurred when the current density at 1 mA/cm^2, showing poor rate capacity and reversibility. For the cells with $Zn(OTf)_2$/GU electrolytes, even after a high-rate charge and discharge of 10 mA/cm^2, when the current density returns to 1 mA/cm^2, the cells can still work well and exhibit excellent reversibility. Symmetric cells assembled with $Zn(OTf)_2$ and $Zn(OTf)_2$/GU electrolytes were subjected to galvanostatic cycling at varying current densities while maintaining a fixed areal capacity of 1.0 mAh/cm^2. As depicted in Fig. 3g, the Zn||Zn symmetric cell employing pure $Zn(OTf)_2$ electrolyte demonstrates limited cycling stability, exhibiting a sudden voltage drop after merely 119 h of operation (Fig. S13 in Supporting information). This premature failure can be attributed to severe Zn dendrite formation and persistent interfacial side reactions at the electrode/electrolyte interface. In striking contrast, the introduction of GU additive confers remarkable stability enhancements owing to multiple synergistic mechanisms including the optimized interfacial between Zn and electrolyte, effective suppression of HER and associated byproducts, and establishes dual H-bond for H_2O molecule confinement. These combined effects enable the GU-modified cell to achieve exceptional cycling stability, maintaining uninterrupted operation for 2160 h at 2 mA/cm^2 with 1 mAh/cm^2 capacity, while com-

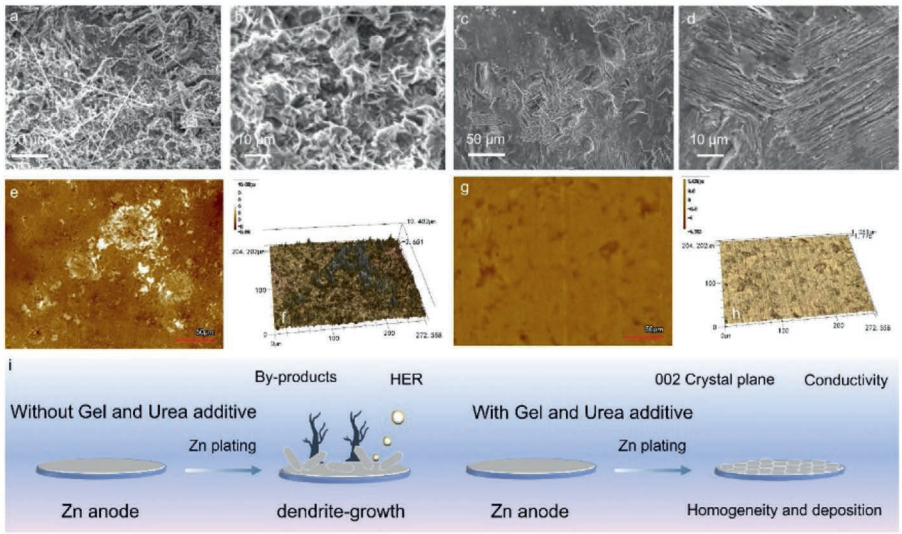


Fig. 4. SEM morphology image of Zn||Zn symmetric cells after 50 cycles (at 2 mA/cm^2 and 1 mAh/cm^2) in (a, b) $Zn(OTf)_2$ and (c, d) $Zn(OTf)_2$/GU electrolytes. Optical microscope images and corresponding height distribution of (e, f) $Zn(OTf)_2$ electrolyte and (g, h) $Zn(OTf)_2$/GU electrolyte after 50 cycles at 2 mA/cm^2 with a capacity of 1 mAh/cm^2. (i) Schematic illustration for the Zn deposition process in different electrolytes.

pared to pure $Zn(OTf)_2$ electrolyte, the system exhibits a remarkably low overpotential, demonstrating exceptional electrochemical kinetics. The dramatic improvement in cycle life underscores the critical role of interfacial engineering in stabilizing Zn metal anodes. The GU additive forms dual cooperative H-bond, effectively locking H_2O molecules within the electrolyte matrix and preventing their participation in side reactions. Magnified views of selected cycles with the $Zn(OTf)_2$/GU electrolytes at a current density of 2 mA/cm^2 and a capacity of 1 mAh/cm^2 in Fig. S14 (Supporting information). The electrochemical performance is mainly evaluated under relatively moderate current densities at high-rate operation is critical for practical Zn metal batteries, we assessed zinc anode cycling stability through long-term Zn||Zn symmetric cell tests. As shown in Fig. S15 (Supporting information), the GU system achieved 500 h cycle life at 5 mA/cm^2 and 1 mAh/cm^2. The charge/discharge voltage profiles remained stable throughout, with no significant polarization increase or sudden voltage drop. As illustrated in Fig. S16 (Supporting information), the exchange current density corresponding to the Zn deposition process under different current densities can be determined. The exchange current density, which reflects the intrinsic redox reaction rate at the equilibrium potential, was determined to be significantly higher for $Zn(OTf)_2$/GU electrolytes (12.04 mA/cm^2) compared to $Zn(OTf)_2$ electrolytes (4.45 mA/cm^2), as derived from linear fitting analysis. This result demonstrates that the $Zn(OTf)_2$/GU system exhibits enhanced Zn deposition kinetics, suggesting a more favorable electrochemical environment for rapid charge transfer during the electroplating process.

Understanding the morphological evolution and preferential growth orientation of metallic zinc during repeated plating/stripping cycles is crucial for the rational design of advanced electrolyte systems. To elucidate the electrolyte-dependent morphological evolution of Zn anodes, scanning electron microscopy (SEM) characterization was performed after 50 cycles at 2 mA/cm^2 and 1 mAh/cm^2. We analyze its morphological evolution under two electrolyte systems. As shown in Figs. 4a and b, the Zn anode cycled in pure $Zn(OTf)_2$ electrolyte exhibits a highly irregular surface morphology characterized by vertically aligned dendritic flakes with random orientations. Notably, the formation of loose sedimentary structures and intrinsic by-products is clearly observed, suggesting an inhomogeneous Zn^{2+} deposition process that leads to unfavorable dendritic growth. More compelling evidence demonstrates that the multifunctional GU additive effectively modulates the electrochemical deposition behavior on the Zn surface, maintaining a remarkably smooth and compact morphology throughout prolonged plating/stripping cycles. Notably, the zinc deposition follows a layered stacking mode, which substantiates the uniform redistribution of Zn^{2+} ions during electrodeposition in Figs. 4c and d. To further investigate the current-dependent morphological evolution, we systematically examined the zinc anode surfaces cycled under at 5 mA/cm^2 and 1 mAh/cm^2 current densities using SEM (Fig. S17 in Supporting information). Strikingly, the samples subjected to higher current conditions exhibited significantly denser and more homogeneous deposition morphologies compared to their low-current counterparts. Comparative analysis revealed that optimal morphological compactness was achieved under moderately elevated current densities. In summary, the SEM characterization thus confirms the preferential growth of the Zn (002) crystal plane and the effective optimization of Zn deposition morphology by the GU additive [41]. XPS was performed on the zinc anode after reaction in $Zn(OTf)_2$/GU electrolytes. As shown in Figs. S18 and S19 (Supporting information), Zn 2p, and C 1s signals could be clearly observed. The C 1s spectrum demonstrates a dominant peak located at ~284.8 eV, which is assigned to the C-H/C-C species. In addition, other peaks are detected and assigned (~286.9 eV for C-O/C-N, and ~293.0 eV for CF_3). To gain deeper insights into the morphological evolution under operational conditions, zinc metal anodes were systematically investigated using laser confocal scanning microscopy (LCSM). As evidenced in Figs. 4e and f, the zinc anodes cycled in $Zn(OTf)_2$ electrolyte exhibits significant surface degradation, and deep voids are clearly visible on the surface of the zinc anode. The non-uniform contours and 3D images verified the irregular peaks and valleys. After a long cycle life of 50 cycles, the anode surface develops severe roughness accompanied by extensive dendritic growth, it confirmed that the extremely uneven Zn deposition behavior on the surface, the random speckled irradiation correlation on the surface and the severe HER in $Zn(OTf)_2$ electrolyte led to the unstable interface behavior. In striking contrast, the GU-modified electrolyte demonstrates remarkable interfacial stabilization, as evidenced by the maintenance of exceptionally smooth and uniform surface morphology even after 50 cycles (Figs. 4g and h). The absence

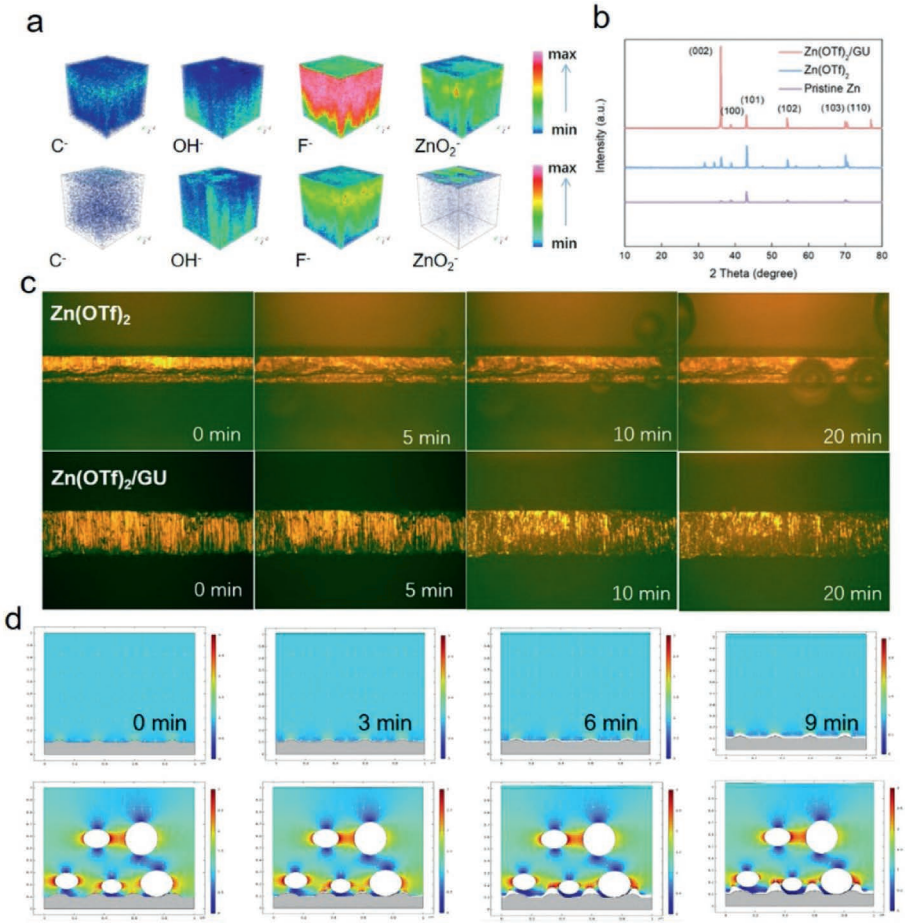


Fig. 5. (a) Three-dimensional view of distributions of Zn sheet after cycled in $Zn(OTf)_2$ and $Zn(OTf)_2$/GU electrolytes in the TOF-SIMS sputtered volumes. (b) XRD patterns of deposited Zn. (c) *In situ* optical microscope images of Zn anode surface deposition using pure $Zn(OTf)_2$ electrolyte (top) and $Zn(OTf)_2$/GU electrolyte (bottom) at a current density of 5 mA/cm^2. (d) COMSOL simulations of dendrite growth and HER models at different times for $Zn(OTf)_2$/GU (top) and $Zn(OTf)_2$ (bottom) electrolytes.

of topological irregularities or dendritic protrusions confirms the effectiveness of GU in regulating Zn^{2+} deposition kinetics and suppressing parasitic side reactions. Based on the above analysis, the regulation mechanism of GU additive on the cycle performance of zinc anodic plating/stripping is shown in Fig. 4i. In conventional $Zn(OTf)_2$ electrolytes, the aqueous-rich interfacial environment on the zinc anode facilitates uncontrolled water-induced side reactions, including HER and corrosion. These parasitic processes not only generate undesirable by-products but also create tip effect that exacerbate dendritic growth. In contrast, the introduction of GU additive establishes a dual H_2O-locking mechanism through H-bond interactions with interfacial H_2O molecules. This unique structure effectively including disrupts the solvation shell of free H_2O molecules, significantly suppressing their adsorption and subsequent decomposition at the electrode surface and modulates the electrochemical double layer structure, guiding uniform Zn^{2+} diffusion and nucleation kinetics. Furthermore, the adsorbed GU molecules preferentially interact with specific zinc crystal planes, favoring the exposure of the (002) crystallographic orientation. This oriented deposition behavior, characterized by parallel Zn platelet alignment, fundamentally prevents dendritic proliferation while enhancing interfacial stability [42,43]. The synergistic combination of water activity suppression and crystallographic control enables the realization of dendrite-free zinc deposition morphology. In summary, the GU additive significantly improves the cycling stability of zinc anodes through a multifaceted mechanism that regulates Zn deposition kinetics, suppresses side reactions, and stabilizes the electrode-electrolyte interface.

To gain deeper insights into the compositional distribution of interfacial byproducts, time-of-flight secondary-ion mass spectrometry (TOF-SIMS) was systematically employed for phase analysis (Fig. 5a). Random distribution of negative ions C^-, OH^-, F^- and ZnO_2^- by-products was detected from the with $Zn(OTf)_2$ and $Zn(OTf)_2$/GU electrolytes. In the electrolyte without additives, the concentration of inorganic substances on the surface of zinc is relatively high. In contrast, the electrolyte containing GU contains minimal of by-products such as ZnO_2^-. The corresponding two-dimensional rainbow plots are distributed in Fig. S20 (Supporting information). X-ray diffraction (XRD) analysis (Fig. 5b) unambiguously confirms the formation of byproducts. They physically obstruct ionic diffusion pathways due to their poor conductivity and induce uneven electric field distribution that promotes dendritic growth, increasing interfacial impedance through discontinuous charge transfer networks. Such unfavorable phase accumulation stands in marked contrast to the homogeneous, conductive interphase formed in GU-modified systems directly correlating with the observed electrochemical performance enhancement. To observe the evolution of the galvanizing process in real time, we adopted an *in-situ* optical microscope. Uniform and dense Zn deposits can be obtained by electroplating in the $Zn(OTf)_2$/GU electrolytes, indicating that electroplating inhibits the growth of dendrites. It can be seen from Fig. 5c that the deposition of zinc in the GU additive is uniform throughout the electroplating process. Conversely, in the $Zn(OTf)_2$ electrolyte, after electroplating for 10 min under the condition of 5 mA/cm^2, a large number of nuclei or protrusions appeared on the zinc surface, obvious protrusions, after

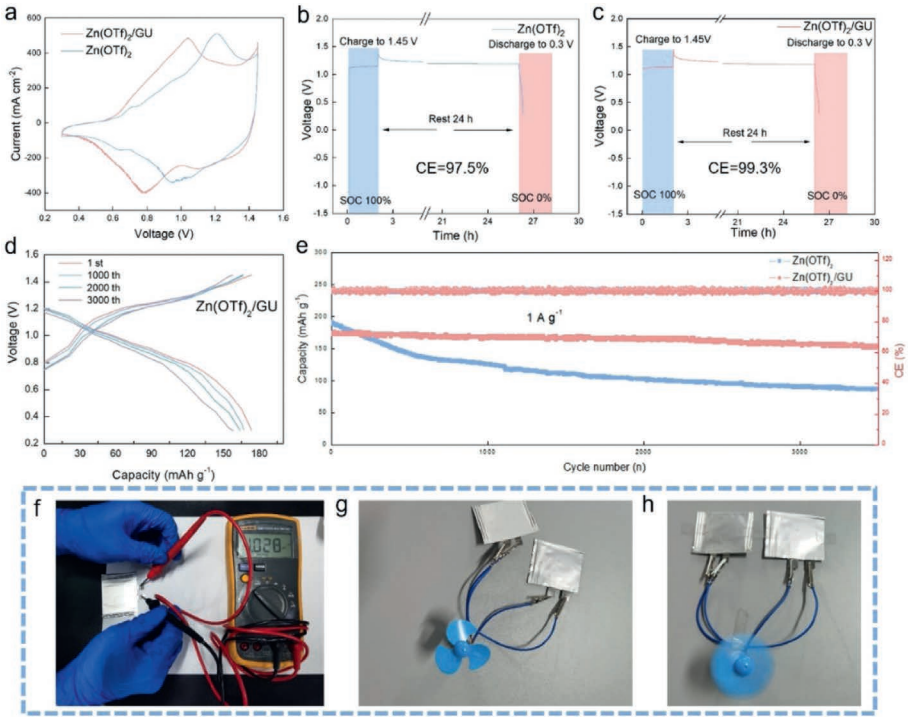


Fig. 6. Electrochemical performances of full cells. (a) CV curves at 1 mV/s. (b) self-discharge behavior of full cell $Zn(OTf)_2$ electrolyte. (c) self-discharge behavior of full cell $Zn(OTf)_2$/GU electrolyte. (d) The charge/discharge curve at 1 A/g of $Zn(OTF)_2$/GU electrolyte. (e) Long-term cycling performance of different cells at 1 A/g. (f) pouch battery voltage diagram. A digital photo shows the power supply for the fan by two Zn||PANI pouch cells in series. (g) Initial state, (h) working status.

electroplating for 20 min finally formed a large number of bubbles and dendrites were eventually produced. In order to deeply explore the influence of GU additive on dendrites, in this study, the finite element simulation theory was adopted to simulate and calculate the zinc ion concentration at the dendrite tip and the deposition interface, as well as the changes in HER in Fig. 5d. The simulation of the electric field and hydrogen distribution by COMSOL confirmed that the presence of GU homogenized the electric field and slowed down the HER. The galvanizing process is uneven, with severe dendrite growth, showing a "tip effect". However, after the introduction of GU, this phenomenon has decreased significantly. The surface of Zn remains relatively flat and the electric field distribution is uniform. In $Zn(OTf)_2$ electrolytes, after electric field-induced diffusion, H^+ accumulates rapidly at the protrusions, and the local concentration flux exceeds the maximum. The H^+ distribution in the adjacent plate areas is relatively thin. After the introduction of GU, the flux on the Zn surface remains uniform, and the concentration flux increases slightly. The results of simulating the electric field and hydrogen distribution confirm that the introduction of GU leads to the homogenization of the electric field and inhibits the evolution of hydrogen. In Fig. S21 (Supporting information), the observed cells swelling after 50 charge-discharge cycles in pure $Zn(OTf)_2$ electrolytes can be attributed to gas evolution during the electrochemical cycling process.

In order to investigate the sufficient practicability of the design of the electrolyte in the H_2O-locking structure strategy, the zinc storage performance in the actual full cells was determined. The full cell was assembled using zinc anode combined with polyaniline (PANI) as the cathode material, and the performance of the constant current charge-discharge full cells was evaluated by $Zn(OTf)_2$ and $Zn(OTf)_2$/GU electrolytes. Cyclic voltammetry (CV) was conducted in the voltage range of 0.3-1.45 V at 1 mV/s (Fig. 6a). Similar peaks in the CV curve indicate that the oxidation-reduction processes were the same with or without the GU additive. Subsequently, the effectiveness of GU additive in inhibiting side reactions was further demonstrated through self-discharge tests (Figs. 6b and c). After standing for 24 h, the CE of the Zn||PANI battery with GU electrolyte was 99.3 %, which was significantly better than 97.5 % of pure $Zn(OTf)_2$ electrolyte. The EIS tests of the full cells with $Zn(OTf)_2$ and $Zn(OTf)_2$/GU electrolytes demonstrate that the $Zn(OTf)_2$/GU electrolytes can deliver a smaller interface impedance, in contrast to the $Zn(OTf)_2$ (Fig. S22 in Supporting information). The corresponding galvanic charge-discharge curves in Fig. 6d and Fig. S23 (Supporting information) for the Zn||PANI full cells in $Zn(OTf)_2$/GU electrolytes illustrate the enhanced reversibility of the electrode reaction. The long-term cycling performance was further evaluated at a current density of 1 A/g. As shown in Fig. 6e, the Zn||PANI cells employing $Zn(OTf)_2$ exhibits rapid capacity decay after 3500 cycles, demonstrating relatively low CE and a poor capacity retention rate of 44.03 %. This performance degradation can be primarily ascribed to uncontrolled Zn dendrite formation and aggravated parasitic side reactions. In contrast, with the $Zn(OTf)_2$/GU electrolytes cells demonstrate remarkable cycling stability 3500 cycles while maintaining exceptional CE exceeding 89.36 %. Moreover, electrochemical characterization reveals that the Zn||PANI cells with $Zn(OTf)_2$/GU electrolytes features a capacitive-dominated charge storage mechanism with rapid kinetics, which contributes to its outstanding rate capability in Fig. S24 (Supporting information). The cells deliver stable performance across a wide range of current densities from 0.1 A/g to 5.0 A/g (0.1, 0.2, 0.5, 1.0, 2.0 and 5.0 A/g), further highlighting the advantages of the $Zn(OTf)_2$/GU electrolytes system. Fig. 6f is a schematic diagram of the voltage of the assembled device. To evaluate the practical application prospects of the GU additive, we assembled a standard Zn||PANI fully charged battery (Figs. 6g and h). The integrated bag-shaped batteries connected in series provide the same energy density. Notably, two connected batteries can easily power a fan, further demonstrating the prospects of GU as an electrolyte additive for AZIBs. From the above experimental results, it can be seen that adding the dual water-locking additive to form

hydrogen bonds with H_2O molecules can effectively extend the cycle life of the Zn anode, and it has good compatibility with the PANI cathode, thus providing an innovative method for the further development of high-performance AZIBs from the PANI cathode.

In summary, GU as the electrolyte additive to inhibit the dendrite growth and side reactions of the Zn anode. Meanwhile, the mutual synergistic effect of the dual additives enables dual regulation of the zinc deposition morphology, resulting in a denser, smoother zinc deposition layer with minimal dendrite formation. The results show that the electrolyte with GU added supports the stable operation of the Zn||Zn symmetric battery for 2160 h under the conditions of 2 mA/cm^2 and 1 mAh/cm^2. In the assembled Zn||Cu asymmetric cells, it operates nearly 1600 times at 5 mA/cm^2 and 1 mAh/cm^2, with a CE of 99.71 %. Impressively, the Zn||PANI full cells assembled with a small amount of zinc demonstrated excellent electrochemical performance with a capacity retention rate of 89.36 % after 3,500 cycles at 1 A/g. These results confirm that GU, as a multifunctional dual additive, can effectively improve the electrochemical performance of AZIBs. Based on the synergistic stabilization strategy constructed with the GU dual additives, provides new insights for the design of high-performance aqueous zinc battery electrolytes. Future work will focus on exploring the practical application potential of this strategy in high-area-capacity pouch cells, thereby advancing its progress toward large-scale energy storage.

CRediT authorship contribution statement

Yang Yu: Writing – original draft, Methodology, Investigation. **Yi-Yang Bi:** Writing – review & editing, Writing – original draft, Investigation. **Yu-Hang Liu:** Validation, Resources, Investigation. **Bin Yue:** Visualization, Supervision, Software. **Ming-Xuan Duan:** Supervision, Investigation, Formal analysis. **Yu-Chun Wan:** Methodology, Investigation, Formal analysis. **Wan-Qiang Liu:** Project administration, Funding acquisition. **Gang Huang:** Methodology, Investigation, Formal analysis.

Declaration of competing interest

The authors declare that they have no known competing financial interests or personal relationships that could have appeared to influence the work reported in this paper.

Acknowledgments

This work was financially supported by the Jilin Province Science and Technology Development Project (No. 20250203128SF). The authors extend their gratitude to Shiyanjia Lab (www.shiyanjia.com) form providing invaluable assistance with the TOF-SIMS analysis and theoretical calculation.

Supplementary materials

Supplementary material associated with this article can be found, in the online version, at doi:10.1016/j.cclet.2026.112540.

Refercnce

[1] Y. Wang, B. Liang, D. Li, et al., Joule 9 (2025) 101944.
[2] Y. Yu, L. Lin, Y.H. Liu, et al., ACS Appl. Mater. Interfaces 17 (2024) 1374–1384.
[3] A. Li, J. Hao, K. Wu, et al., ACS Nano 19 (2025) 13016–13028.
[4] S. Hazoor, Y. Tang, R. Luo, et al., Adv. Funct. Mater. 35 (2025) e10936.
[5] J. Lin, C. Ji, G. Guo, et al., Angew. Chem. Int. Ed. 64 (2025) 202501721.
[6] X. Yu, M. Chen, J. Wang, et al., Nat. Commun. 16 (2025) 3820.
[7] X. Wang, W. Zhou, L. Wang, et al., Adv. Mater. 37 (2025) 202501049.
[8] X. Liu, X. Nie, Y. Yang, et al., Chem. Sci. 16 (2025) 6918–6929.
[9] T. Jiang, D. Shen, Z. Zhang, et al., Nat. Rev. Clean Technol. 1 (2025) 474–492.
[10] Y. Ouyang, W. Zong, X. Gao, et al., Angew. Chem. Int. Ed. 64 (2025) e202504965.
[11] H. Ni, Z. Fan, J. Wang, et al., Energy Storage Mater. 77 (2025) 104220.
[12] W. Wang, Z. Li, W. Li, et al., Chem. Eng. J. 512 (2025) 162304.
[13] R. Luo, X. Zheng, T. Jiang, et al., Adv. Energy Mater. 15 (2025) 2501658.
[14] J. Kumankuma-Sarpong, C. Chang, J. Hao, et al., Adv. Mater. 36 (2024) 2403214.
[15] G. Cao, L. Zhao, X. Ji, et al., Small 19 (2023) 2207610.
[16] K. Wang, H. Zhan, W. Su, et al., Energy Environ. Sci. 18 (2025) 1398–1407.
[17] R. Qin, Y. Wang, M. Zhang, et al., Nano Energy 80 (2021) 105478.
[18] H. Wang, S. Deng, S. Wang, et al., Angew. Chem. Int. Ed. 64 (2025) e202422395.
[19] Y. Li, H. Xu, X. Xuan, et al., Chem. Eng. J. 505 (2025) 158934.
[20] Y. Wang, T. Wang, S. Bu, et al., Nat. Commun. 14 (2023) 1828.
[21] Q. Zhang, X. Gao, K. Liu, et al., Commun. Chem. 7 (2024) 173.
[22] H. Lin, L. Zeng, C. Lin, et al., Energy Enviro. Sci. 18 (2025) 1282–1293.
[23] Q. Xiao, S. He, P. Liu, et al., Adv. Funct. Mater. 35 (2024) 202417708.
[24] S.J. Guo, M.Y. Yan, D.M. Xu, et al., Energy Environ. Sci. 18 (2025) 418–429.
[25] J. Luo, L. Xu, Y. Zhou, et al., Angew. Chem. Int. Ed. 62 (2023) e202302302.
[26] Q. Kang, H. Liang, Z. Zhu, et al., Angew. Chem. Int. Ed. 64 (2025) e202420183.
[27] S. An, L. Hu, X. Li, et al., Energy Storage Mater. 64 (2024) 103076.
[28] T. Xue, Y. Mu, Z. Zhang, et al., Adv. Energy Mater. 15 (2025) 202500674.
[29] Z. Zhu, T. Jiang, M. Ali, et al., Chem. Rev. 122 (2022) 16610–16751.
[30] Y. An, C. Shu, Y. Liu, et al., ACS Nano 19 (2025) 11146–11163.
[31] Y. Xia, Y. Xiao, J. Zhang, et al., Adv. Funct. Mater. 35 (2025) 2500889.
[32] X. Yang, W. Li, Z. Chen, et al., Angew. Chem. Int. Ed. 62 (2023) e202218454.
[33] H. Wang, W. Ye, B. Yin, et al., Angew. Chem. Int. Ed. 62 (2023) e202218872.
[34] Z. Xiao, X. Dai, J. Zhu, et al., Adv. Funct. Mater. 35 (2025) 202424860.
[35] Q. Gou, H. Luo, Q. Zhang, et al., Small 19 (2023) 2207502.
[36] Y. Wei, H. Wang, X. Lin, et al., Energy Environ. Sci. 18 (2025) 786–798.
[37] F. Wu, J. Zhang, L. Ma, et al., Angew. Chem. Int. Ed. 64 (2025) e20241787.
[38] Y. Yu, L. Lin, Z.Y. Hu, et al., J. Colloid Interface Sci. 689 (2025) 137251.
[39] K. Lu, C. Chen, Y. Wu, et al., Chem. Eng. J. 457 (2023) 141287.
[40] Y. Niu, L. Chang, Q. Sun, et al., ACS Appl. Mater. Interfaces 16 (2024) 6988–6997.
[41] N. Yu, S. Lin, S. Zhou, et al., Energy Storage Mater. 80 (2025) 104398.
[42] G. Weng, Y. Su, J. Huang, et al., Adv. Energy Mater. 14 (2024) 2401293.
[43] X. Yang, Y. Lu, Z. Liu, et al., Energy Enviro. Sci. 17 (2024) 5563–5575.